

Research



Cite this article: Ord A, Hobbs B, Dering G, Gessner K. 2018 Nonlinear analysis of natural folds using wavelet transforms and recurrence plots. *Phil. Trans. R. Soc. A* **376**: 20170257. <http://dx.doi.org/10.1098/rsta.2017.0257>

Accepted: 26 April 2018

One contribution of 13 to a theme issue 'Redundancy rules: the continuous wavelet transform comes of age'.

Subject Areas:

geology

Keywords:

natural geological fold systems, nonlinear dynamical systems, multifractal geometry, wavelet transform, recurrence quantification, Hurst exponents

Author for correspondence:

Alison Ord

e-mail: alison.ord@uwa.edu.au

Nonlinear analysis of natural folds using wavelet transforms and recurrence plots

Alison Ord^{1,2}, Bruce Hobbs^{1,3}, Greg Dering¹ and Klaus Gessner¹

¹Centre for Exploration Targeting, School of Earth Sciences, University of Western Australia, 35 Stirling Highway, Crawley, Western Australia 6009, Australia

²School of Resources and Environmental Engineering, Hefei University of Technology, Hefei 230009, People's Republic of China

³CSIRO, 26 Dick Perry Avenue, Kensington, Western Australia 6151, Australia

A0, 0000-0003-4701-2036

Three-dimensional models of natural geological fold systems established by photogrammetry are quantified in order to constrain the processes responsible for their formation. The folds are treated as nonlinear dynamical systems and the quantification is based on the two features that characterize such systems, namely their multifractal geometry and recurrence quantification. The multifractal spectrum is established using wavelet transforms and the wavelet transform modulus maxima method, the generalized fractal or Renyi dimensions and the Hurst exponents for longitudinal and orthogonal sections of the folds. Recurrence is established through recurrence quantification analysis (RQA). We not only examine natural folds but also compare their signals with synthetic signals comprising periodic patterns with superimposed noise, and quasi-periodic and chaotic signals. These results indicate that the natural fold systems analysed resemble periodic signals with superimposed chaotic signals consistent with the nonlinear dynamical theory of folding. Prediction based on nonlinear dynamics, in this case through RQA, takes into account the full mechanics of the formation of the geological system.

This article is part of the theme issue 'Redundancy rules: the continuous wavelet transform comes of age'.

1. Introduction

When layered rocks are shortened during tectonic events, the most obvious structures formed are folds. Folding of layered rocks causes a change in geological structure that can lead to a fundamental modification of the mechanical and hydraulic properties of the rock mass across several orders of magnitude in length—typically from the millimetre to the kilometre scale. The understanding of how, why and on which scale folding occurs therefore has fundamental implications for problems in geology and engineering, including prediction of the form and location of hydrocarbon accumulations [1], salt domes [2], groundwater flow [3], mineralization [4,5] and rock slope stability [6–8].

The buckling phenomenon which generates these folds is important mathematically and has received considerable attention over the past decades [9–18]. It involves the shortening of a layered material.

The buckling process itself has generally been described in a form of Swift–Hohenberg equation:

$$\alpha \frac{\partial^4 w}{\partial x^4} + \beta \frac{\partial^2 w}{\partial x^2} + f(w) = 0,$$

where w is the deflection of the layer, x is a distance from some origin along the layer and $f(w)$ is a function which describes the resistance exerted by the matrix on the deflecting layer. If $f(w)$ is linear, then one solution to the Swift–Hohenberg equation is $f(w) = \sin x$. However, in this case, because the system is linear, any superposition of periodic functions ($A \sin x + B \cos x$) is also a solution to the equation. An important contribution was made by Biot [19] in showing that one wavelength (the dominant wavelength) grows faster than all others, so that the finite-time solution to the linear equation is always periodic. Some [20,21] have claimed that irregularities observed in natural folds arise because the dispersion function is not strongly peaked and many of the periodic or quasi-periodic¹ solutions possible for the linear Swift–Hohenberg equation are preserved in nature.

However, localized folds arising from nonlinearity form in a fundamentally different way than the Biot wavelength selection process [9–18]. If $f(w)$ is not linear, then there are an indefinite number of solutions to the Swift–Hohenberg equation, many of them localized [10–14,16]. Hence, for the nonlinear system, departures from periodicity are to be expected, independently of the presence of initial imperfections or of the development of a broad dispersion function. In the nonlinear system, the energy landscape consists of a number of intertwined surfaces and the evolving buckling system can jump from one of these surfaces to another so that in some instances the layer does not buckle simultaneously everywhere as predicted from the linear Biot theory but undergoes sequential fold development [18,22–26]. The very first solution (as the amplitude starts to grow) is a Biot solution [9]. There is then a very early bifurcation that leads to a localized solution. From then on, the system switches from one energy branch to another, adding new localized deflections to each bifurcation. Thus, one might expect the final system to be a Biot solution (that is, periodic) with many superimposed chaotic packets.

This paper explores the geometry of some natural three-dimensional folds in order better to understand the dynamics associated with these systems. As the general nonlinear system may be chaotic, we expect natural folds to exhibit many of the features of nonlinear dynamical systems. This includes, in particular, the development of multifractal geometries and recurrence phenomena. By ‘chaotic’ in this context, we mean systems that are deterministic, of finite size and whose behaviour is sensitive to initial conditions. Beck & Schlögl [27] point out that, because the attractor for chaotic systems comprises an indefinite number of singularities, multifractal geometry is a natural consequence as an expression of the entropy of the system. Poincaré [28] pointed out that, for any nonlinear dynamical system, the trajectories in phase space that describe the evolution of the system must repeatedly become arbitrarily close to each other, thus resulting in recurrence [29].

¹We use quasi-periodic in its strict mathematical sense to mean functions of the form $y = A \sin x + B \cos x$, where the ratio A/B is an irrational number.

We have prepared three-dimensional models of natural fold systems using photogrammetry and we explore the multifractal geometry using the wavelet transform modulus maxima (WTMM) method [30–34] and recurrence quantification [29,35–37] in order to delineate the dynamics of naturally folded systems. We show for comparison numerical results of quasi-periodic signals and Hénon mappings. The property of interest with the Hénon low two-dimensional mapping, as well as its mechanical underpinning, is its possession of a strange attractor, of interest to geology and naturally occurring fold systems because it was suggested that they may display spatial chaos in their geometry [8,38]. The Lorenz model and its strange attractor, the basis for weather exploration, is associated with three- or higher-dimensional dynamical systems [27].

2. Methods

(a) Tools

The tools required for analysis must be able to discriminate between patterns arising from linear and from nonlinear processes. The characterization of nonlinear systems in terms of multifractal geometry and recurrence in the dynamics constitutes an important toolbox for many physical, chemical, biological [34,39], geological [40–45] and climate [29,46–48] systems.

In the linear case, Fourier analysis describes the distribution of wavelengths (or frequencies) of superimposed periodic signals; the law of superposition holds for the description of the patterns in terms of sine and cosine, that is, as a sum of trigonometric functions. A fundamental frequency may be determined, with integer multiples of this frequency being understood as harmonics. Such a process has been used to attempt to describe as well as analyse the shapes of folded rocks [26,49–51]. The general determination of recurrence, however, describes the distribution of wavelengths of any type of signal, non-periodic, that is, signals for which the law of superposition does not hold, as well as periodic. The wavelet transform approach allows determination of such non-integer multiples of frequencies in a signal. The attractor for a periodic system is always a regular torus. The distribution of singularities on the attractor is ‘smooth’ and the resulting singularity spectrum for a perfect sine curve is a single point. The attractor for a non-periodic system is more complicated; the distribution of singularities on the attractor when considered within the framework of statistical mechanics [27] results in a multifractal singularity spectrum.

(b) Wavelet transform modulus maxima method

(i) Background

The WTMM method was introduced in the 1990s [30–33,52] to address limitations of the box-counting and structure-function methods in testing various multiplicative cascade models and exploring velocity fluctuations in turbulence data analysis [34]. The box-counting method has been much developed for exploration of scaling laws in geology, including ore deposit distributions [53–59], mineral prospectivity [60–63], ore resource estimation [64] and assessing the relationship between ore grade and tonnage [65]. Ord *et al.* [66] began to develop a model of a mineralizing system as an open flow reactor operating far from equilibrium given a continuing supply of reactants and energy, with Lester *et al.* [67] exploring the processes leading to the efficient mixing of fluids and the consequences for producing multifractal ore-grade distributions. Lester *et al.* [67] first introduced the work of Arneodo *et al.* [52] to understanding mineralizing systems, noting their use of wavelet analysis with a thermodynamic foundation. Arneodo *et al.* [52] (see also [68]) show that it is possible to extract from data some information on the nature of the dynamical system responsible for the data, in particular, the origin of the multiplicative hierarchical structure of some multifractals. Such studies, therefore, hold the potential for increasing the understanding behind ore-grade distributions and in particular discovering if there is intrinsic structural order underlying what appears to be an irregular distribution of ore grades

rather than simply restricting one's considerations as to whether the ore distribution is spatially isotropic or anisotropic. This approach has since been developed by Ord *et al.* [41] and Munro *et al.* [44], with Munro *et al.* [44] concluding that wavelet-based analysis of routinely acquired hyperspectral reflectance signals is effective for quantifying the dynamical organization of down-hole primary mineralization, host rock alteration, and vein and breccia infill mineralogy, and for comparing and contrasting the dynamic associations within the different mineralogies.

Hobbs & Ord [40] enlarge the concept to include deforming rocks in general, using wavelet transforms for quantification of deformation/metamorphic fabrics and patterns, including the distribution of mineral phases, the crystallographic preferred orientations developed during deformation, the geometry of fracture and vein networks, and the shapes of folds at all scales. They provide initial wavelet analyses, which are both fast and convenient, including the wavelet scalogram (two- and three-dimensional) for orthogonal sections across deformed quartzites, across computational models for shearing, and across fold structures. They also comment on the Legendre transform and its usefulness in expressing the relationships between the singularity spectrum and a measure of the scaling exponent for the generalized fractal dimension [52] and thermodynamic potentials.

(ii) Details

In exploring multifractal geometries, it is convenient to define the generalized fractal dimension, D_q , which is related to the scaling exponent for the q th moment of the measure μ . If we have a set of measures, say the concentration of a chemical component such as Ca distributed over a fabric, we define the q th moment (or partition function) $\mathbb{Z}(q, \varepsilon)$ for the box size ε as [69]

$$\mathbb{Z}(q, \varepsilon) = \sum_{i=1}^{N(\varepsilon)} \mu_i^q(\varepsilon). \quad (2.1)$$

Then we can also define $\tau(q)$ as

$$\tau(q) = \lim_{\varepsilon \rightarrow 0} \frac{\ln \mathbb{Z}(q, \varepsilon)}{-\ln \varepsilon}. \quad (2.2)$$

The generalized fractal or Renyi dimensions D_q are given by

$$\tau(q) = D_q(1 - q). \quad (2.3)$$

In the limit $\varepsilon \rightarrow 0^+$, (q, ε) behaves as a power law,

$$\mathbb{Z}(q, \varepsilon) \sim \varepsilon^{-\tau(q)}. \quad (2.4)$$

The relationships between the $f(\alpha)$ singularity spectrum, q and the $\tau(q) = (1 - q)D_q$ spectrum are given [52] by

$$q = \frac{df(\alpha)}{d\alpha},$$

$$\frac{d^2f(\alpha)}{d\alpha^2} < 0$$

and

$$\tau(q) = q\alpha - f(\alpha).$$

A discussion of the WTMM formalism is given in Hobbs & Ord ([40], pp. 235–239).

The parameters are obtained from decomposing a signal, \hat{s} , into space-scale contributions which are defined by the analysing wavelet, ψ . Successive derivatives of the Gaussian function,

$$\psi(x) = g^{(N)}(x) = (-1)^{N+1} \frac{d^N}{dx^N} \left[\exp\left(\frac{-x^2}{2}\right) \right],$$

represent a class of commonly used wavelets. Wavelets $g^{(2)}$, otherwise known as the Mexican hat wavelet courtesy of its evocative shape (figure 1a), and $g^{(3)}$ (figure 1b) are used in the analyses represented here. The chosen wavelet (the 'mother' wavelet) is scanned across the image, with

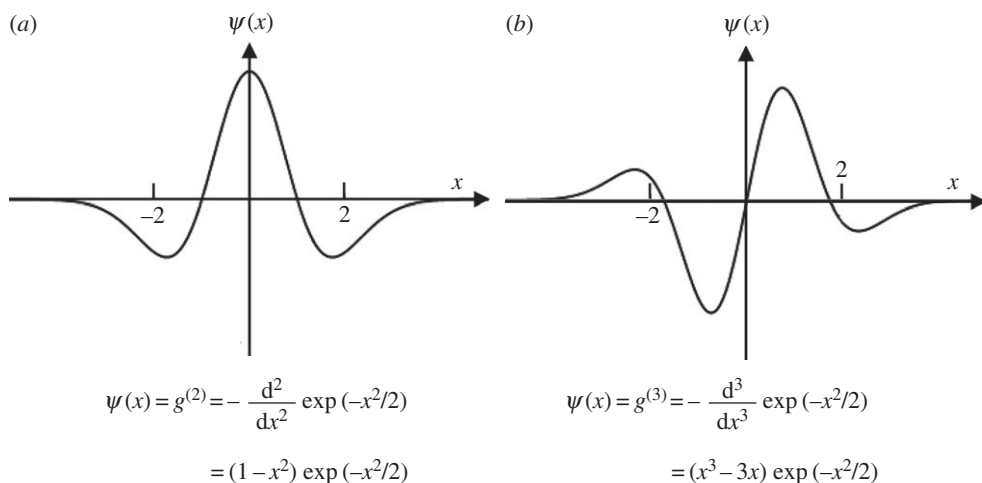


Figure 1. Analysing wavelet, form and equation. (a) The second derivative of the Gaussian, $g^{(2)}$ (Mexican hat wavelet). (b) The third derivative of the Gaussian, $g^{(3)}$.

ψ contracted or expanded by successive scales a . The wavelet transform (WT) is defined as the convolution of $\bar{\psi}$ with \hat{s} , providing the wavelet coefficient at the scale a and around the point $x=b$, for b a space parameter, $a > 0$ the scale parameter, and $\bar{\psi}$ the complex conjugate of ψ . The wavelet transform thus reflects the local behaviour of the signal. Figure 2a shows a signal, in this case representing the height of a rock along a single transect. The Mexican hat wavelet was scanned across the data, for $b=0-1250$, represented by the x -axis in figure 2b, and scale a from 0 to 32, represented by the y -axis in figure 2b. The magnitude of the wavelet coefficient at each point (x, y) for each b and for each a is represented by a point of colour in figure 2b, with blue representing low magnitudes and red representing high magnitudes. See appendix A for further details. The partition function (which relates macroscopic properties to the microscopic details of a system) is then evaluated at each point (b, a) (or (x, y)) of the wavelet transform with only the maximum terms noted (figure 2c), the ‘modulus maxima’ method. The q th-order moments $M(a, q)$ are calculated through a wavelet-based moment function $M(a, q) = \sum_i |T(a, b_i)|^q$, where $|T(a, b_i)|$ is the i th WTMM found at scale a . Such partitioning for a multifractal object results in a function with power-law behaviour, $M(a, q) \propto a^{\tau(q)}$. Application of the Legendre transform simply changes the independent variables in this function by application of the product rule. It converts from a function of one set of variables to another function of a conjugate set of variables. This results in this case in definition of the function $f(\alpha)$ (figure 2d), the dimension spectrum of the fractal set with a particular singularity strength α , $f(\alpha) = \min_q (q\alpha - \tau(q))$, thus characterizing the multifractal system being explored.

(iii) Application

The LASTWAVE[®] software [34] (LASTWAVE 3.1, ©1998–2008 E. Bacry, lastwave@cmap.polytechnique.fr) has been used here to calculate various measures of the singularity spectrum (see also table 3), including the box dimension D_0 (where the subscript is the value for q described above), the information dimension D_1 , the correlation dimension D_2 , and D_∞ and $D_{-\infty}$, using as analysing wavelet the successive derivatives of the Gaussian function (in general $g^{(2)}$ or $g^{(3)}$ as noted). The maximum range of q explored was from -40 to $+40$. In general the singularity spectra were symmetric in form, in contrast to asymmetries observed in the minerals and elements observed in rock drill core [44]. The wavelet scalogram (derived from MATHEMATICA[®] as well as from LASTWAVE) is particularly useful for comparison of details of the strength of the spectrum at varying scales.

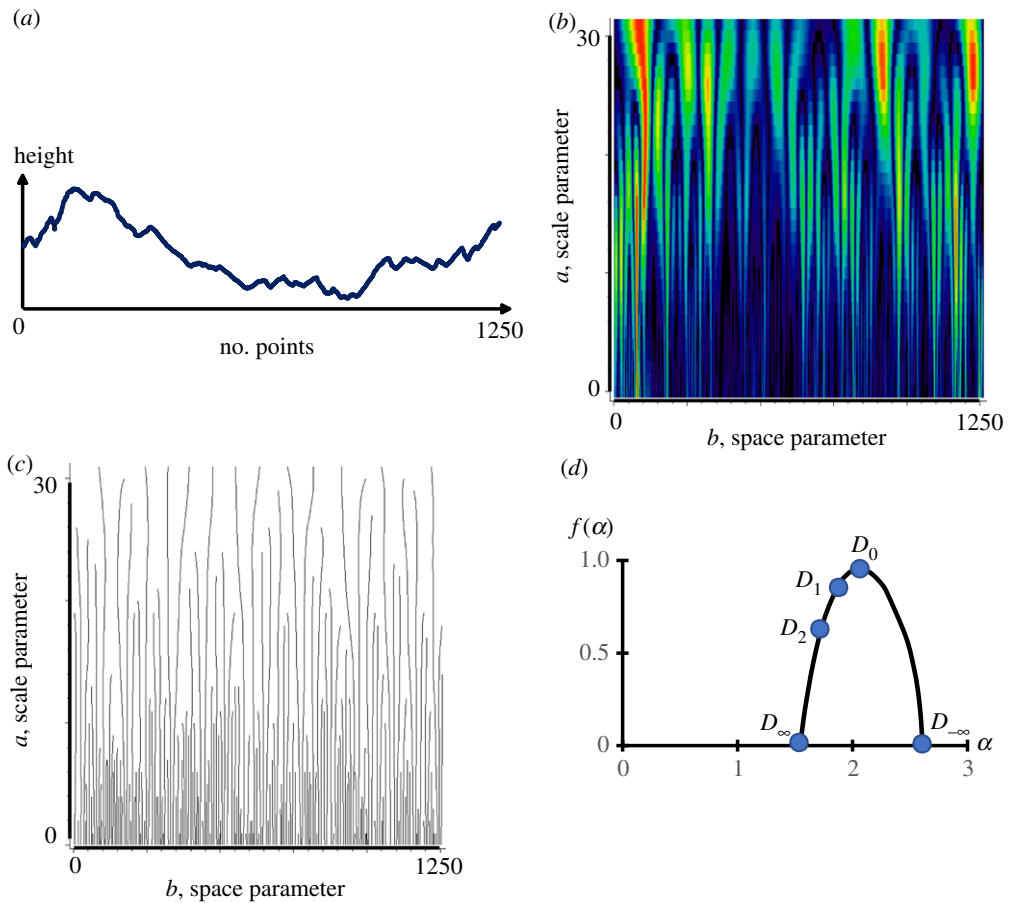


Figure 2. Multifractal spectrum of the one-dimensional topography of a rock. (a) The signal. (b) Wavelet transform or scalogram of the signal (a) using the Mexican hat wavelet. (c) Skeleton of maxima lines from the wavelet scalogram (b) using LASTWAVE. (d) The multifractal or singularity spectrum, $f(\alpha)$ versus α , resulting from partitioning of the wavelet modulus maxima (LASTWAVE), with various measures (D_q) noted (see also table 3).

Spatial correlations are also determined using the Hurst exponent [46,47,70,71] to explore the wavelet transform at a number of spatial scales. See Liu *et al.* [58] for use of the Hurst exponent in exploring the spatial distributions of various ore-forming elements.

(c) Recurrence quantification analysis

An important concept in nonlinear analysis is the recurrence plot (RP) [35]; this contains all the information that defines the underlying dynamics of a system. An RP determines the times (or locations for a spatially patterned signal) at which a trajectory in phase space visits roughly the same area in that phase space. It is represented for a one-dimensional dataset by a symmetrical matrix, R_{ij} , expressed as a two-dimensional visualization and defined by

$$R_{ij} = \Theta(\varepsilon - \|x_i - x_j\|) \quad \text{for } i, j = 1, \dots, N, \quad (2.5)$$

where ε is an arbitrary threshold distance that measures the radius within which recurrence is identified, Θ is the Heaviside function and $\|*\|$ denotes a norm, commonly taken as the Euclidean norm. Equation (2.5) says that we measure the distance between a given point, x_i , on the signal and every other point, $j = 1$ to N , on the signal and give that measure the value

Table 1. Measures used in RQA.

recurrence rate	%REC Percentage of recurrent points falling within radius, ε , for W , number of points in signal.
determinism	%DET Percentage of recurrent points forming diagonal line structures; predictability of the system
DMAX	Length of the longest diagonal line. The shorter the line, the faster the divergence of the phase space trajectory.
entropy	The Shannon information entropy of probability distribution of the diagonal line lengths. Complexity of deterministic structures.
trend	A measure of system stationarity.
laminarity	%LAM Percentage of recurrent points forming vertical line structures; intermittency of system.
VMAX	Length of the longest vertical line.
trapping time	TT Average length of vertical line structures. Length of time (or space) system remains in a specific state.

Table 2. Significance of patterns in recurrence plots.

pattern	significance
homogeneous	The process is stationary. TREND tends to zero. TREND tends to infinity for a heterogeneous distribution.
fading pattern to upper right or lower left	Non-stationary data; the process contains a trend or drift.
disruptions (horizontal or vertical)	Non-stationary data; some states are far from the normal; transitions may have occurred. %LAM reflects such intermittency.
periodic or quasi-periodic patterns	The process is cyclic. The vertical (or horizontal) distance between periodic lines corresponds to the period. Variations in the distance means quasi-periodicity in the process. For example, simple periodic systems have all diagonal lines of equal length; entropy tends to zero.
single isolated points	Represent rarity or strong fluctuations in the process. The process may be uncorrelated or anti-correlated. e.g. white noise has almost only single dots; low DET.
diagonal lines (parallel to the line of identity, LOI)	The evolution of the system is similar over the length of the line. If lines appear next to single isolated points, the process may be chaotic. For example, sine waves give very long diagonal lines; chaotic signals give many very short diagonal lines.
diagonal lines (orthogonal to the LOI)	The evolution of states at different times is similar but with reverse timing.
vertical and horizontal lines or clusters	States do not change with time or change slowly; represented by trapping time.
lines not parallel to the LOI - sometimes curved	The evolution of states is similar at different times but the rate of evolution changes with time. The dynamics of the system is changing with time.

1 if the distance is within the radius ε , or 0 if not. This is repeated for all values of $i=1$ to N to form the recurrence matrix. The caveat is that the distances are measured in the embedding space of the attractor for the system. As described by Takens [72] *the complete dynamics of a system can be derived from a time (or spatial) series for a single state variable from that system*, so that the dynamics of the system are encompassed by the attractor for that system. An RP is then a plot

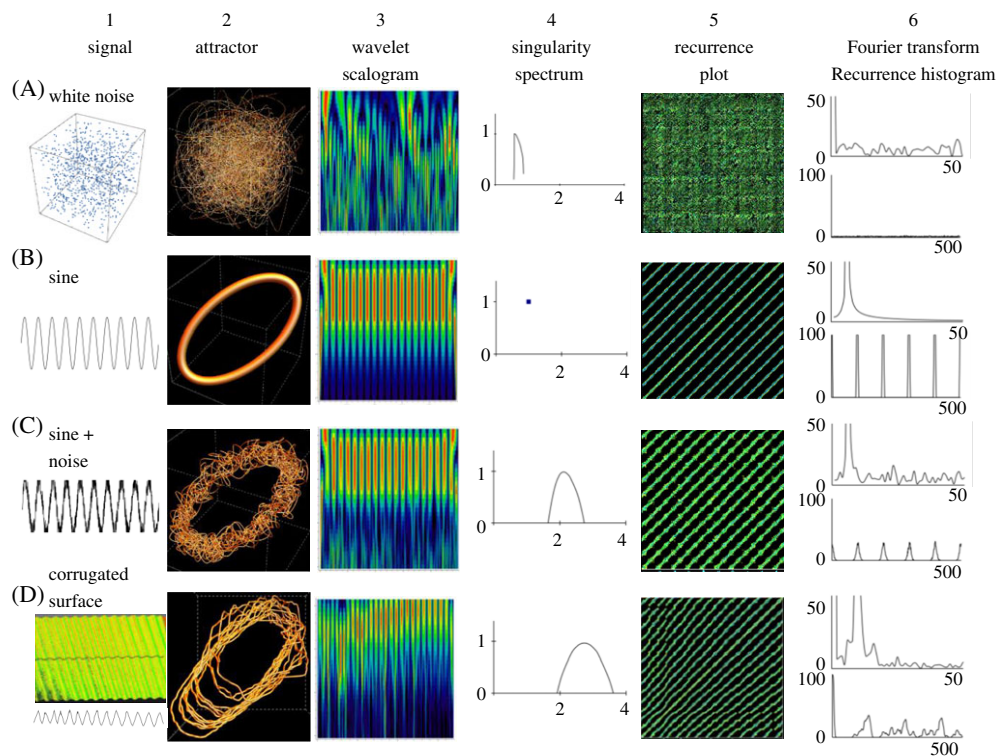


Figure 3. Row A White noise. Row B Sine. Row C Sine plus noise. Row D Corrugated surface. Column 1 Signal. Column 2 Attractor. Column 3 Two-dimensional wavelet scalogram. Column 4 Singularity spectrum. Column 5 Recurrence plot. Column 6 Upper: Fourier transform, Lower: Recurrence histogram.

of R_{ij} and may be contoured according to different values of ε . Recurrence plots may also be constructed for higher-dimensional data [37,73]; however, if the data exist in d dimensions, the RP is in $2d$ space. The application of recurrence plots in the geosciences (except for climate studies) is rare; some examples are the application to alteration mineralogy in drill core [42,45] and to global navigation satellite system data [43]. The input data are not constrained to any type of statistical distribution and the data are not required to be stationary. There is no need to know the mathematical rules (if any) governing the system under study. The work of Webber [74] and Kononov [75] has resulted in easily accessible software (RQA and VRA, respectively). The quantification of recurrence plots has been developed by Webber & Zbilut [36] and a summary of the various quantification measures with their significance is given in tables 1 and 2.

3. Observations

Figures 3, 4 and 6 each have six columns (1–6) over four rows (A–D, E–H, I–L). The rows represent data and analyses for various signals, synthetic and measured. Column 1 displays the signal for each row; column 2 the attractor (for a delay of 10 and an embedding dimension of 3; displayed using MATHEMATICA); column 3 the wavelet scalogram (using LASTWAVE); column 4 the singularity spectrum (derived from LASTWAVE); column 5 the RP (using RQA); and column 6 the fast Fourier transform (upper; from EXCEL®), and the recurrence histogram (lower; using VRA).

(a) Synthetic and manufactured fold signals

In figure 3, row A is for white noise, row B is for $\sin(x)$, and row C is for $\sin(x)$ plus noise. The data are those provided with the RQA software [74] (WHITE, SINE and SINENOIS).

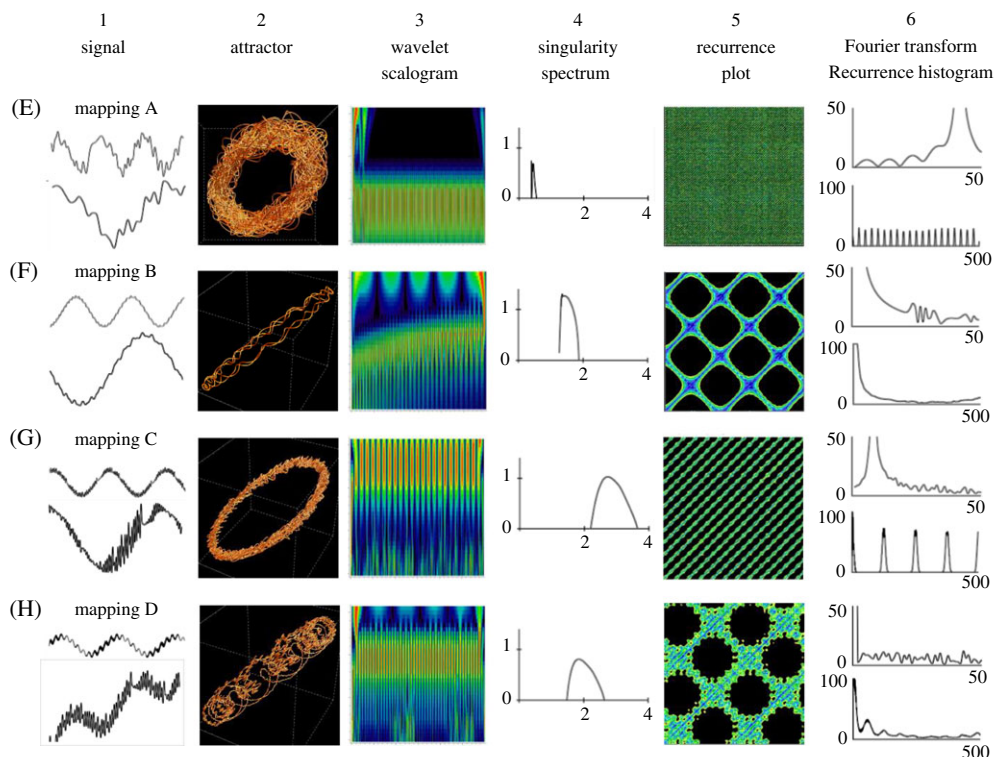


Figure 4. Row E Mapping A. Row F Mapping B. Row G Mapping C. Row H Mapping D. Column 1 Signal (at two scales to show details). Column 2 Attractor. Column 3 Two-dimensional wavelet scalogram. Column 4 Singularity spectrum. Column 5 Recurrence plot. Column 6 Upper: Fourier transform, Lower: Recurrence histogram.

Row D represents a signal (obtained through photogrammetry) across an engineered corrugated surface with a wavelength of 2.5 cm. It is important that the method used for determining the measures for those theoretically perfectly sinusoidal surfaces is the same as that used for determining the measures for naturally deformed surfaces. The image shows the cloud of points describing the surface in CloudCompare (<http://www.cloudcompare.org>), with the trace of the signal oriented east–west, orthogonal to the axial plan of the corrugations, and through the central region.

(b) Functions that describe nonlinear signals

Figure 4 displays nonlinear quasi-periodic and chaotic signals. Rows E, F, G and H are all calculated within EXCEL. The equations for each signal are as follows, with J as the y -axis and n as the x -axis.

Row E: Mapping A, quasi-periodic

$$J = \sin(0.25n) + 0.25 \sin(50\sqrt{(n2)}) + 0.25 \sin(50\sqrt{(n7)}).$$

Row F: Mapping B, quasi-periodic

$$J = \sin(0.01n) + 0.05 \sin(7.5\sqrt{(n2)}) + 0.025 \sin(7.5\sqrt{(n7)}).$$

The next two mappings are based on eqns 6.1 and 6.2 of Sprott [71] and a sample strange attractor from his fig. 6.1. The base mapping is

$$\begin{aligned} X_{n+1} &= a_1 + a_2 X_n + a_3 Y_n + a_4 X_n^2 + a_5 X_n Y_n + a_6 Y_n^2, \\ Y_{n+1} &= X_n. \end{aligned}$$

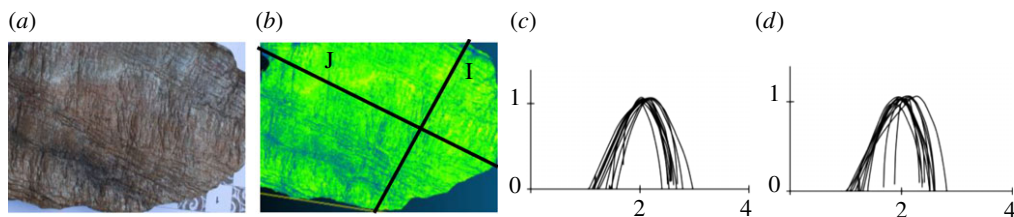


Figure 5. Willyama folded rock. (a) The rock. (b) Visualization of surface of rock through a cloud of points in three dimensions. Note section lines I and J. (c) Singularity spectra for 12 sections parallel to line I. (d) Singularity spectra for 11 sections parallel to line J.

The initial condition is $X_0 = Y_0 = 0.05$, with parameters $a_1 = 0.0$, $a_2 = -0.4$, $a_3 = 1.7$, $a_4 = 1.1$, $a_5 = -3.3$ and $a_6 = 0.0$.

This results [71] in Lyapunov exponents of 0.195 and -0.530 and a Kaplan–Yorke dimension of 1.368. Fig. 6.2 of Sprott [71] displays a map of a versus b demonstrating the existence of chaotic as well as periodic dynamical behaviours for this Hénon mapping.

Row G: Mapping C, periodic plus chaotic

$$J = \sin(0.05n) + 0.5X_{n+1} \quad \text{where } n = 1, 2, 3, \dots$$

Row H: Mapping D, periodic plus chaotic

$$J = \sin(0.01n + 0.3X_{n+1}) + 0.25 \sin(0.0725n\sqrt{2}) + 0.2X_{n+1} \quad \text{where } n = 1, 2, 3, \dots$$

(c) Naturally deformed rocks

Figure 6, rows I, J, K and L display signals for three large hand samples of naturally deformed rocks. For each sample, the topography of a deformed surface was digitally reconstructed using 20–30 JPEG images processed using digital photogrammetry techniques with the commercial software AGISOFT PHOTOSCAN Pro® (<http://www.agisoft.com>). The accuracy of three-dimensional point clouds produced using digital photogrammetry techniques has been shown to be similar to laser scanning techniques applied to hand specimens [76]. The folded surfaces were rendered as dense point clouds with an effective surface sampling resolution of 0.5 mm. The analysed signal was derived from two-dimensional topographic profiles that sampled the surface corrugations. Examples of topographic profiles are shown in figure 6, column 1, rows I, J, K and L.

Figures 5 and 6, rows I and J, Willyama mica schist. The first rock, referred to as Willyama, is shown in figure 5a, and its cloud in CloudCompare in figure 5b. In the latter image, there are two lines, I and J, and their derived signals are shown in figure 6, row I and row J, respectively. Figure 5c shows singularity spectra for 12 lines parallel to I across the rock; figure 5d shows singularity spectra for 11 lines parallel to J across the rock. The rock itself is about 25 by 30 cm in size. It was collected from a multiply deformed (egg box style) area in Broken Hill, Australia (NW Willyama Complex [77]; see especially their fig. 7). Conditions for the deformation and metamorphism are inferred to range from 550°C to 650°C, and 300 to 500 MPa confining pressure. As well as folds at the millimetre, centimetre and decimetre scales, in the field, the rocks are folded also at the metre and 10 m scales.

Figure 6, row K, Rum Jungle graphite schist. The second rock, from (and named) Rum Jungle, Northern Territory, Australia, is shown in row K. It has multiple corrugations running approximately east–west in the figure, which are apparently overlain by finer corrugations running approximately north–south. Conditions for deformation and metamorphism are suggested to be greenschist facies, or about 250°C, 200–300 MPa confining pressure. The sample surface is about 20 × 20 cm.

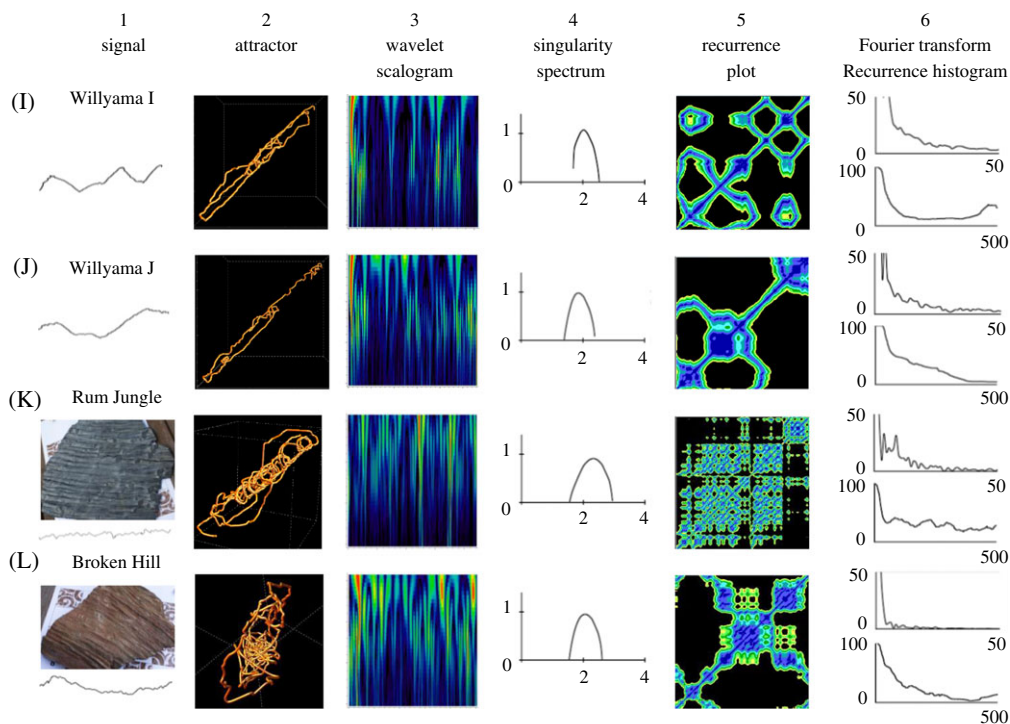


Figure 6. Row I Willyama section I. Row J Willyama section J. Row K Rum Jungle rock. Row L Broken Hill rock. Column 1 Signal. Column 2 Attractor. Column 3 Two-dimensional wavelet scalogram. Column 4 Singularity spectrum. Column 5 Recurrence plot. Column 6 Upper: Fourier transform, Lower: Recurrence histogram.

Figure 6, row L, Broken Hill mica schist. The third rock (figure 6, row L) is also from Broken Hill, but from a different region than the rock in figure 5. Similar conditions are inferred for the deformation and metamorphism. It is gently folded about an axis roughly northwest–southeast in the photo, with many corrugations running also in the same direction. The sample surface is about 15×10 cm.

See appendix B for details for columns, for figures 3, 4 and 6.

4. Discussion

The wavelet scalogram and the RP appear to be the best discriminants between any periodic signal and naturally formed folds (figures 3, 4 and 6). At a first glance, perhaps row A, column 3 and row L, column 3 are similar. However, the attractors (column 2), the singularity spectra (column 4), the recurrence plots (column 5) and the recurrence histograms are quite different. It is hardly surprising that the wavelet scalograms (column 3) for the sine signal (row B), the sine + noise signal (row C) and the corrugated surface (row D) are similar to those for mapping C (row G) and mapping D (row H). However, the cross-bars in the RP for mapping D (row H, column 5) are quite distinctive and separate out the mapping D signal from all the other numerically simulated signals, as well as from the engineered corrugated surface. This pattern of cross-bars is seen also for signal mapping B (row F, column 5). It appears also, though not nearly so regularly, for the signals of Willyama I (row I, column 5), Willyama J (row J, column 5) and Broken Hill (row L, column 5). The fast Fourier transforms (column 6, upper panel) for the four rocks (rows I, J, K and L) most resemble that for signal mapping B (row F). The recurrence histograms (column 6, lower panel) for the four rocks (rows I, J, K and L) most resemble those for signal mapping B (row F) and mapping D (row H). The attractors (column 2) for the rocks (rows I, J, K and L) are most similar to those for mapping B (row F) and mapping D (row H).

Table 3. Measures of the singularity spectra.

Data set	D_0	D_1	D_2	D_{∞}	$D_{-\infty}$	D_1/D_0	D_2/D_0	$D_{-\infty} - D_{\infty}$
white noise	n/a							
Sine	n/a							
Sine + noise	0.99	0.93	0.78	1.7	2.8	0.94	0.79	1.1
Mapping A	0.68	0.53	0.68	0.4	0.5	0.78	1.00	0.1
Mapping B	1.27	1.31	1.24	1.3	1.9	1.03	0.98	0.6
Mapping C	1.03	0.96	0.77	2.2	3.6	0.93	0.75	1.4
Mapping D	0.81	0.75	0.64	1.5	2.7	0.93	0.79	1.2
Corrugated	0.97	0.78	0.35	1.9	3.6	0.80	0.36	1.7
Rum Jungle	0.91	0.73	0.25	1.5	2.9	0.80	0.28	1.4
Broken Hill	0.95	0.87	0.68	1.5	2.6	0.92	0.72	1.1
Willyama I sections	1.00- 1.08	0.29-1.01	-0.09- 0.80	1.1- 1.70	2.10- 3.00	0.29- 0.94	-0.09- 0.74	0.80-1.90
Willyama J sections	0.98- 1.07	0.58-1.00	-0.28- 0.97	1.00- 1.90	2.30- 2.80	0.56- 0.96	-0.27- 0.93	0.60-1.70

Table 4. Results of RQA for an assumed embedding dimension of 3 and a delay of 10.

Data set	%REC	%DET	DMAX	Entropy	Trend	%LAM	VMAX	TT
white noise	9.2	17.1	6	0.5	-0.6	19.7	4	2.1
Sine	17	100	979	3.5	-3.8	99.9	21	15.2
Sine + noise	18.3	82.8	142	3.0	-3.1	87.3	30	6
Mapping A	18.8	79.7	225	2.7	0.34	89.5	10	3.9
Mapping B	32.2	100	1479	6.5	9.44	100	274	96.4
Mapping C	21.8	79.5	1479	4.5	-0.81	83.5	45	17.7
Mapping D	35.2	87.8	1479	6.0	12.17	91.4	261	50
Corrugated	22	99.3	1674	6.2	0.4	99.9	62	25.4
Rum Jungle	47.4	99.9	2187	7.6	-43.1	100	754	101.1
Broken Hill	40.2	99.9	1241	7.6	-56.4	100	592	121.8
Willyama I sections	35.4- 45.8	99.93- 99.98	1339- 1641	6.04- 8.43	-78.6- 23.9	99.97- 100	365-839	131-246
Willyama J sections	32.2- 43.4	99.93- 99.99	1143- 1543	6.73- 8.36	-89.7- -6.78	99.97- 100	459-748	137-215

The singularity spectra do not appear to be good discriminants (table 3), unlike a separate mineralogical study on drill core [44]. Certainly, the ranges of all measures are similar for all the rocks. The patterns of the associated wavelet scalogram (figure 6, column 3) bring out the different scales of the folds very clearly, delineating and quantifying the finer structures.

Some of the recurrence measures (table 4), on the other hand, appear to be excellent discriminants, particularly the Trend for which the very low range is unique to the rocks. The ranges for %REC, VMAX and TT (trapping time) are common to the rocks and to mapping B and mapping D. The remaining measures do not discriminate between the various mappings and the rocks.

The Hurst exponents (figure 7), derived for the different scales of the wavelet scalogram [41], become important for determination of long-range correlations (for Hurst exponent greater than 0.5), a signature for nonlinear systems, and their use in measuring uncertainty in prediction for the folds at that particular scale. Note how the Hurst exponent discriminates the rocks, with

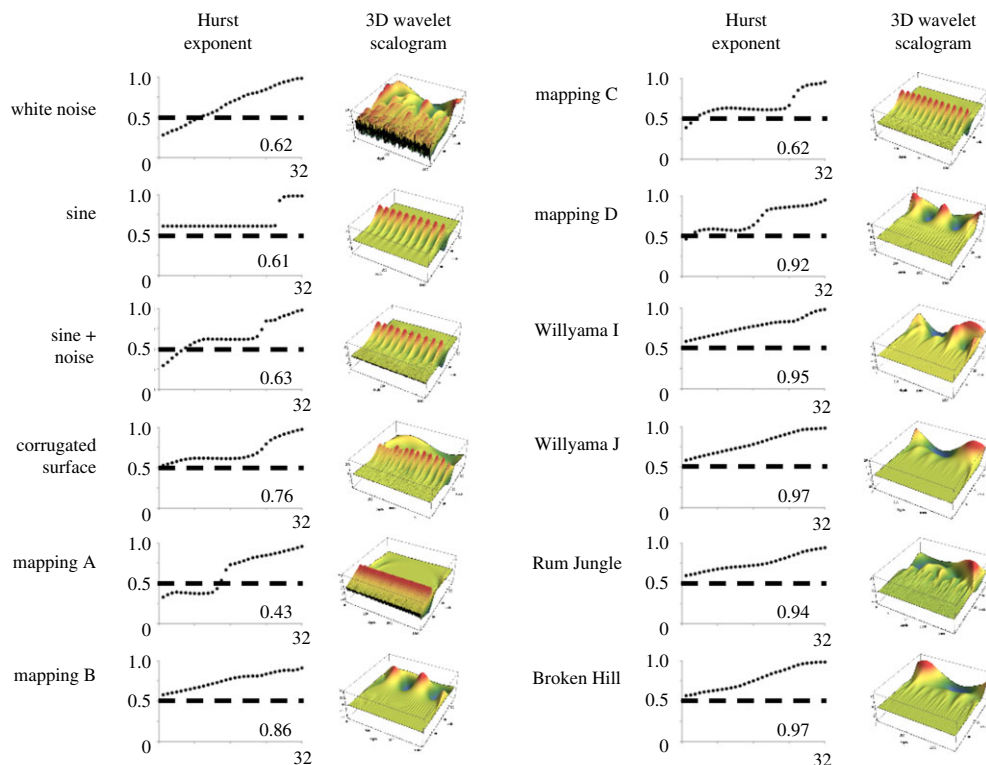


Figure 7. Columns 1 and 3. Measures of the Hurst exponents (y -axis, 0–1, horizontal dashed line denotes a Hurst exponent of 0.5) at different scales (x -axis, 0–32). Columns 2 and 4. Three-dimensional wavelet scalogram (z -axis represents the wavelet coefficient). Column 1, from the top down: white noise, sine, sine plus noise, corrugated surface, mapping A, mapping B. Column 2, from the top down: mapping C, mapping D, Willyama I, Willyama J, Rum Jungle, Broken Hill. The number on each figure in columns 1 and 3 is the Hurst exponent for each complete signal.

Hurst exponents of 0.94–0.97. Mapping D has a Hurst exponent of 0.92, mapping B has a Hurst exponent of 0.86, followed by the corrugated surface at 0.76. White noise, sine, sine plus noise and mapping C have Hurst exponents between 0.61 and 0.63, while that for mapping A is a low 0.43.

Overall, the measures for the rocks are unique, with those for mapping D being closest.

This issue of prediction is explored further for the Willyama I section (figure 8). Figure 8*a* shows how the system is trained over the first 1100 points of the signal; the signal between 1150 and 1400 points is then predicted and the results are shown in figure 8*b*. This prediction is based on nonlinear dynamics, in this case through recurrence quantification analysis (RQA), and takes into account the full mechanics of the formation of the geological system. Even better predictive methods are available [78] and should be explored for their considerable potential.

5. Conclusion

The three-dimensional structures of the three rocks analysed are not perfectly periodic, nor are they periodic with only superimposed noise but periodic with superimposed chaotic packets. The recurrence measures, particularly Trend, followed by %REC, VMAX and the trapping time, and the Hurst exponents for the signal, best discriminate the rocks from the numerical signals; the states change slowly and long-range correlations exist at all scales. Mapping D, a mix of periodic and chaotic signals, compares best with the rocks. Quantification of the structures using tools

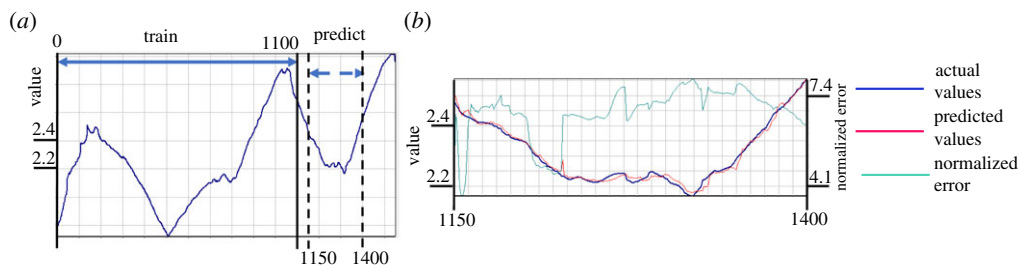


Figure 8. The Willyama I signal is used to test nonlinear training and prediction. The non-parametric modelling for nonlinear time-series prediction of VRA based on the radial basis function model, using the delay of 10 and embedding dimension of 3 used for the recurrence plots in figures 3, 4 and 6, is applied to the Willyama section I data. Panel (a) shows the original signal (Willyama section I, figure 5b; figure 6, row I); the system is trained over the first 1100 points, and then predicted from point 1150 to point 1400. Panel (b) shows the original values (blue) and the predicted values (red) which visually appear remarkably close to the actual values. That visual closeness is quantified by the normalized error (green, noted on the right-hand axis). The root mean square error is 0.0115.

of analysis for nonlinear dynamics, therefore, demonstrates the nonlinear, and possibly chaotic, nature of the structures. The three-dimensional structures most resemble periodic signals with superimposed chaotic signals. This is consistent with the nonlinear theory of folding which says that the very first solution (as the amplitude starts to grow) is a Biot solution. There is a very early bifurcation that leads to a localized solution. From then on, the system switches from one energy branch to another, adding new localized deflections to each bifurcation. Thus, one might expect the final system to be a Biot solution (that is, periodic) with many superimposed chaotic packets. Such intriguing relationships require further research.

Prediction based on nonlinear dynamics, in this case through RQA, takes into account the full mechanics of the formation of the geological system. Even better predictive methods are available [78]; they should be explored for their considerable potential for improving cross-section construction, three-dimensional modelling, and other approaches to addressing big data issues in geological and engineering problems; issues that are of major economic impact in hydrocarbon production, mineral exploration and engineering geology.

Data accessibility. This article has no additional data.

Authors' contributions. A.O. made substantial contributions to the conception and design of the manuscript, to the acquisition of data, and to the analysis and interpretation of data; she drafted the original article as well as revising it critically for important intellectual content; and provided final approval of the version to be published. B.H. made substantial contributions to the conception and design of the manuscript, as well as to the interpretation of the data; he revised drafts critically for important intellectual content; and provided final approval of the version to be published. G.D. made substantial contributions to acquisition and analysis of data, revised the article critically for important intellectual content, and provided final approval of the version to be published. K.G. made substantial contributions to acquisition and analysis of data, revised the article critically for important intellectual content, and provided final approval of the version to be published.

Competing interests. The authors declare we have no competing interests.

Funding. No external sources funded the development of this manuscript.

Acknowledgements. We thank Paul Addison, Tom Blenkinsop and Jorn Kruhl for their helpful suggestions for improvement of the manuscript.

Appendix A

In MATHEMATICA a scaling parameter, s , of the wavelet signal is defined in terms of an equal tempered scale given in powers of 2 and divided into octaves and subdivided into four 'voices'.

Thus, the scaling parameter is divided into the array expressed in (A 1).

$$\begin{array}{ll}
 [1, 1], [1, 2], [1, 3], [1, 4] & \text{octave 1, voices 1 to 4} \\
 [2, 1], [2, 2], [2, 3], [2, 4] & \text{octave 2, voices 5 to 8} \\
 \dots\dots\dots & \\
 [n_{\text{oct}}, 1], [n_{\text{oct}}, 2], [n_{\text{oct}}, 3], [n_{\text{oct}}, 4] & \text{octave } n_{\text{oct}}, \text{ voices } (4n_{\text{oct}} - 3) \text{ to } 4n_{\text{oct}},
 \end{array} \quad (\text{A } 1)$$

where n_{oct} is the total number of octaves representing the wavelet signal and is given by

$$n_{\text{oct}} = \left\lfloor \log_2 \left(\frac{n}{2} \right) \right\rfloor,$$

where n is the number of data points in the signal (equally spaced) and $\lfloor x \rfloor$ is the floor to x , that is, the largest integer smaller than x . Thus, for $n = 240$, $n_{\text{oct}} = 6$. If n is the number of data points for height across an irregular surface n millimetres long, then n is expressed in millimetres.

The smallest wavelet scale, α_{scale} , for the analysing wavelet ($g^{(2)}$, also known as the Mexican hat wavelet courtesy of its distinctive shape) is given by

$$\alpha_{\text{scale}} = \left[\left(2\pi \sqrt{\frac{2}{5}} \right) \sigma \right]^{-1},$$

where σ is the width of the hat, taken to be equal to one so that $\alpha_{\text{scale}} = 0.25165$ units. The units correspond to those used to measure the distance between points. The scaling parameter for a particular octave and voice is given by

$$s_{\text{octave,voice}} = \alpha_{\text{scale}} 2^{\text{octave}-1} 2^{\text{voice}/n_{\text{voice}}},$$

where, in MATHEMATICA, n_{voice} is taken to be 4 so that

$$s_{1,1} = 0.25165 \times 2^{1-1} 2^{1/4} = 0.299359,$$

and each successive voice differs from the one smaller by a factor of $2^{1/4}$ or 1.19.

Thus, if the signal consists of 240 points each 1 mm apart, $n_{\text{oct}} = 6$ and the array (A 1) becomes

$$\begin{array}{ll}
 [0.299359], [0.355881], [0.423217], [0.503292] & \text{octave 1, voices 1 to 4} \\
 [0.598519], [0.711763], [0.846433], [1.00658] & \text{octave 2, voices 5 to 8} \\
 [1.19704], [1.42353], [1.69287], [2.01317] & \text{octave 3, voices 9 to 12} \\
 [2.39407], [2.84705], [3.38574], [4.02634] & \text{octave 4, voices 13 to 16} \\
 [4.78815], [5.6941], [6.77146], [8.05267] & \text{octave 5, voices 17 to 20} \\
 [9.5763], [11.3882], [13.5429], [16.1053] & \text{octave 6, voices 21 to 24.}
 \end{array} \quad (\text{A } 2)$$

In this case, the voices, in square brackets, are expressed in millimetres.

The vertical axis on the scalogram can be represented by the array (A 1) or as (A 2) or more simply by just the octaves, numbered 1 to n_{oct} , or the voices, numbered 1 to n_{voice} . In this paper, we use only the voices, but to convert scales to millimetres, as in the Hurst exponent measurements, the above discussion is relevant.

Appendix B

Column 1: Signal

Figure 3. Row A. White noise contains 1000 points with a range of 0 to +1 in y . Row B. The sine signal contains 1000 points with a range of -1 to +1 in y . Row C. Sine noise contains 1000 points, also with a range of -1 to +1 in y . The signal for the corrugated surface (row D) contains 1696 points, with a range in y (and now also height) of 0.38–1.16.

Figure 4. Row E. Mapping A contains 1500 points of which the upper signal shows 0–80, with a range in y of -1.5 to +1.5. Row F. Mapping B contains 2000 points of which 1500

(from 500 to 2000) are shown (upper signal), with a range in y of about -1.1 to $+1.1$. The fast Fourier transform (FFT) analyses 1024 points, from 477 to 1500 inclusive. Row G. Mapping C contains 1500 points of which the upper signal shows 150–450 to display the detail; the range is about -1 to 1.5 in y . Row H. Mapping D contains 1500 points, with a range (upper signal) of about -1.2 to $+1.4$ in y . The lower signal in each case is a zoom into part of the upper signal.

Figure 6. The signal for section I (figure 5*b*; figure 6, row I; Willyama) contains 1552 points over a profile distance of about 25 cm, with a range in height (y) of about 1.7–3 cm. The J signal (figure 5*b*; figure 6, row J; Willyama) contains 1407 points, with a height (y) range of about 2–3.6 cm over a profile distance of about 30 cm. The signal for the finely corrugated and essentially flat rock from Rum Jungle (row L) contains 2209 points (the FFT is still only for the first 1024 points) with a range in height (y) of about 0.5–1.4 cm (profile distance 20 cm). The signal for the more coarsely folded rock with corrugations from Broken Hill (row M) contains 1263 points with a range in height (y) of about 1.2–1.5 cm (profile distance 15 cm).

Column 2: Attractor

Column 3: Wavelet scalogram

The y -axis or scale in each case runs from 32 at the top to 0 at the origin at the bottom. The x -axis represents the number of points, increasing to the right from zero at the left-hand origin. In most cases, the maximum value on the x -axis represents the number of points represented in the signal. For mapping A and mapping B, the maximum value on the x -axis is 1500.

Column 4: Singularity spectrum

The axes are marked with 1 on the y -axis, 0 at the origin, and 2 and 4 on the x -axis. The points analysed in each case are the same as those analysed in the wavelet scalogram. Table 3 provides the measures of the box dimension D_0 , the information D_1 , the correlation dimension D_2 , and D_∞ and $D_{-\infty}$ for each signal.

Column 5: Recurrence plot

The x - and y -axes have as their maximum almost the number of points per signal as described for the wavelet scalogram and singularity spectrum. The total number of points analysed is always slightly less according to the magnitude of the embedding dimension and of the delay used in running recurrence quantification display [74]. Table 1 defines the RQA measures while table 4 provides RQA measures for the signals analysed.

Column 6: Recurrence histogram

The recurrence histogram (VRA) for the signal forms the lower panel, with 0 at the origin, a maximum of 100 for the y -axis and 500 for the x -axis. The *Fast Fourier Transform* (EXCEL 2016, Microsoft Office 365) forms the upper panel, with 0 at the origin, and a maximum of 50 for each axis. In the case of the FFT, the analysis is over the first 512 or 1024 points of the sequence (according to whether the signal contains 1000 or 1500 or more points and unless noted otherwise).

References

1. Mitra S. 1990 Fault-propagation folds: geometry, kinematic evolution, and hydrocarbon traps (1). *AAPG Bull.* **74**, 921–945.
2. Talbot CJ, Jackson MP. 1987 Internal kinematics of salt diapirs. *AAPG Bull.* **71**, 1068–1093.
3. Ben-Itzhak LL, Gvirtzman H. 2005 Groundwater flow along and across structural folding: an example from the Judean Desert, Israel. *J. Hydrol.* **312**, 51–69. (doi:10.1016/j.jhydrol.2005.02.009)
4. Cox SF, Wall VJ, Etheridge MA, Potter TF. 1991 Deformational and metamorphic processes in the formation of mesothermal vein-hosted gold deposits—examples from the Lachlan Fold Belt in central Victoria, Australia. *Ore Geol. Rev.* **6**, 391–423. (doi:10.1016/0169-1368(91)90038-9)

5. Schaub PM, Wilson CJ. 2002 The relative roles of folding and faulting in controlling gold mineralization along the Deborah Anticline, Bendigo, Victoria, Australia. *Econ. Geol.* **97**, 351–370. (doi:10.2113/gsecongeo.97.2.351)
6. Brideau MA, Yan M, Stead D. 2009 The role of tectonic damage and brittle rock fracture in the development of large rock slope failures. *Geomorphology* **103**, 30–49. (doi:10.1016/j.geomorph.2008.04.010)
7. Stead D, Wolter A. 2015 A critical review of rock slope failure mechanisms: the importance of structural geology. *J. Struct. Geol.* **74**, 1–23. (doi:10.1016/j.jsg.2015.02.002)
8. Hobbs BE. 1993 The significance of structural geology in rock mechanics. In *Comprehensive rock engineering*, vol. 1 (eds E Hoek, J Hudson, ET Brown), chapter 2, pp. 25–62. Oxford, UK: Pergamon Press.
9. Muhlhaus H-B. 1993 Evolution of elastic folds in plane strain. In *Modern approaches to plasticity* (ed. D Kolymbas), pp. 734–765. New York, NY: Elsevier.
10. Hunt GW, Muhlhaus H-B, Whiting IM. 1996 Evolution of localized folding for a thin elastic layer in a softening visco-elastic medium. *Pure Appl. Geophys.* **146**, 229–252. (doi:10.1007/BF00876491)
11. Hunt G, Muhlhaus H-B, Hobbs B, Ord A. 1996 Localised folding of viscoelastic layers. *Geol. Rundsch.* **85**, 58–64. (doi:10.1007/s005310050052)
12. Hunt GW, Muhlhaus H-B, Whiting IM. 1997 Folding processes and solitary waves in structural geology. *Phil. Trans. R. Soc. Lond. A* **355**, 2197–2213. (doi:10.1098/rsta.1997.0118)
13. Peletier MA. 2001 Sequential buckling: a variational analysis. *SIAM J. Math. Anal.* **32**, 1142–1168. (doi:10.1137/S0036141099359925)
14. Peletier MA, Troy WC. 2001 *Spatial patterns: higher order models in physics and mechanics*. Progress in Nonlinear Differential Equations and Their Applications, vol. 45. Boston, MA: Birkhauser.
15. Hunt GW. 2006 Buckling in space and time. *Nonlinear Dyn.* **43**, 29–46. (doi:10.1007/s11071-006-0748-8)
16. Hobbs BE, Regenauer-Lieb K, Ord A. 2008 Folding with thermal–mechanical feedback. *J. Struct. Geol.* **30**, 1572–1592. (doi:10.1016/j.jsg.2008.09.002)
17. Knobloch E. 2008 Spatially localised structures in dissipative systems: open problems. *Nonlinearity* **21**, T45–T60. (doi:10.1088/0951-7715/21/4/T02)
18. Hobbs BE, Ord A. 2012 Localized and chaotic folding: the role of axial plane structures. *Phil. Trans. R. Soc. A* **370**, 1966–2009. (doi:10.1098/rsta.2011.0426)
19. Biot MA. 1965 *Mechanics of incremental deformations*. New York, NY: John Wiley.
20. Fletcher RC. 1974 Wavelength selection in folding of a single layer with power law rheology. *Am. J. Sci.* **274**, 1029–1043. (doi:10.2475/ajs.274.9.1029)
21. Hudleston PJ, Treagus SH. 2010 Information from folds: a review. *J. Struct. Geol.* **32**, 2042–2071. (doi:10.1016/j.jsg.2010.08.011)
22. Ramsay JG. 1967 *Folding and fracturing of rocks*. New York, NY: McGraw-Hill.
23. Watkinson AJ. 1976 Fold propagation and interference in a single multilayer unit. *Tectonophysics* **34**, T37–T42. (doi:10.1016/0040-1951(76)90092-5)
24. Watkinson AJ, Cobbold PR. 1978 Localization of minor folds by major folds. *Geol. Soc. Am. Bull.* **89**, 448–450. (doi:10.1130/0016-7606(1978)89<448:LOMFBM>2.0.CO;2)
25. Hudleston PJ. 1986 Extracting information from folds in rocks. *J. Geol. Educ.* **34**, 237–245. (doi:10.5408/0022-1368-34.4.237)
26. Johnson AM, Fletcher RC. 1994 *Folding of viscous layers*. New York, NY: Columbia University Press.
27. Beck C, Schlögl F. 1995 *Thermodynamics of chaotic systems*. New York, NY: Cambridge University Press.
28. Poincaré H. 1890 Sur le problème des trois corps et les équations de la dynamique. *Acta Mathematica* **13**, 1–271.
29. Marwan N, Roman MC, Thiel M, Kurths J. 2007 Recurrence plots for the analysis of complex systems. *Phys. Rep.* **438**, 237–329. (doi:10.1016/j.physrep.2006.11.001)
30. Muzy JF, Bacry E, Arneodo A. 1991 Wavelets and multifractal formalism for singular signals: application to turbulence data. *Phys. Rev. Lett.* **67**, 3515–3518. (doi:10.1103/PhysRevLett.67.3515)

31. Bacry E, Muzy JF, Arneodo A. 1993 Singularity spectrum of fractal signals from wavelet analysis: exact results. *J. Stat. Phys.* **70**, 635–674. (doi:10.1007/BF01053588)
32. Muzy JF, Bacry E, Arneodo A. 1993 Multifractal formalism for fractal signals: the structure–function approach versus the wavelet-transform modulus-maxima method. *Phys. Rev. E* **47**, 875–884. (doi:10.1103/PhysRevE.47.875)
33. Muzy JF, Bacry E, Arneodo A. 1994 The multifractal formalism revisited with wavelets. *Int. J. Bifurcation Chaos Appl. Sci. Eng.* **4**, 245–302. (doi:10.1142/S0218127494000204)
34. Arneodo A, Audit B, Kestener P, Roux S. 2008 Wavelet-based multifractal analysis. *Scholarpedia* **3**, 4103. (doi:10.4249/scholarpedia.4103)
35. Eckmann J-P, Kamphorst SO, Ruelle D. 1987 Recurrence plots of dynamical systems. *Europhys. Lett.* **4**, 973–977. (doi:10.1209/0295-5075/4/9/004)
36. Webber Jr CL, Zbilut JP. 2005 Recurrence quantification analysis of nonlinear dynamical systems. In *Tutorials in contemporary nonlinear methods for the behavioral sciences*, ch. 2 (eds MA Riley, GC Van Orden), pp. 26–94. See <https://www.nsf.gov/pubs/2005/nsf05057/nmbs/nmbs.pdf>.
37. Marwan N, Kurths J, Saperin P. 2007 Generalised recurrence plot analysis for spatial data. *Phys. Lett. A* **360**, 545–551. (doi:10.1016/j.physleta.2006.08.058)
38. Ord A. 1994 The fractal geometry of patterned structures in numerical models for rock deformation. In *Fractals and dynamic systems in geoscience* (ed. JH Krühl), pp. 131–155. Berlin, Germany: Springer.
39. Addison AS. 2005 Wavelet transforms and the ECG: a review. *Physiol. Meas.* **26**, R155–R199. (doi:10.1088/0967-3334/26/5/R01)
40. Hobbs BE, Ord A. 2015 *Structural geology: the mechanics of deforming metamorphic rocks*. Amsterdam, The Netherlands: Elsevier.
41. Ord A, Munro M, Hobbs BE. 2016 Hydrothermal mineralising systems as chemical reactors: wavelet analysis, multifractals and correlations. *Ore Geol. Rev.* **79**, 155–179. (doi:10.1016/j.oregeorev.2016.03.026)
42. Oberst S, Niven R, Ord A, Hobbs B, Lester D. 2017 Application of recurrence plots to orebody exploration data. In *TARGET 2017, Perth, Australia: abstracts*, Geological Survey of Western Australia, record 2017/6 (eds S Wyche, WK Witt), pp. 114–116.
43. Hobbs BE, Ord A. In press. Nonlinear dynamical analysis of GNSS data: quantification, precursors and synchronization. *Prog. Earth Planet. Sci.*
44. Munro MA, Ord A, Hobbs BE. 2018 Spatial organization of gold and alteration mineralogy in hydrothermal systems: wavelet analysis of drillcore from Sunrise Dam Gold Mine, Western Australia. In *Characterization of ore-forming systems from geological, geochemical and geophysical studies*. Geological Society, London, Special Publications, vol. 453 (eds K Gessner, TG Blenkinsop, P Sorjonen-Ward). London, UK: Geological Society. (doi:10.1144/SP453.10)
45. Oberst S, Niven R, Lester D, Ord A, Hobbs B, Hoffmann N. In press. Detection of unstable periodic orbits in mineralizing geological systems. *Chaos*.
46. Arneodo A, Audit B, Decoster N, Muzy J-F, Vaillant C. 2002 Wavelet based multifractal formalism: applications to DNA sequences, satellite images of cloud structure and stock market data. In *The science of disasters: climate disruptions, heart attacks and market crashes* (eds A Bunde, A Kropp, HJ Schellnhuber), pp. 26–102. Berlin, Germany: Springer.
47. Arneodo A, Decoster N, Kestener P, Roux S. 2003 A wavelet-based method for multifractal image analysis: from theoretical concepts to experimental applications. In *Advances in imaging and electron physics*, vol. 126 (ed. PW Hawkes), pp. 1–92. San Diego, CA: Academic Press. (doi:10.1016/S1076-5670(03)80014-9)
48. Marwan N, Schinkel S, Kurths J. 2013 Recurrence plots 25 years later—gaining confidence in dynamical transitions. *Europhys. Lett.* **101**, 20007. (doi:10.1209/0295-5075/101/20007)
49. Harbaugh JW, Preston FW. 1965 *Fourier series analysis in geology*, 46 p. University of Arizona, College of Mines, Tucson.
50. Stabler CL. 1968 Simplified Fourier analysis of fold shapes. *Tectonophysics* **6**, 343–350. (doi:10.1016/0040-1951(68)90049-8)
51. Hudleston PJ. 1973 Fold morphology and geometrical implications of theories of fold development. *Tectonophysics* **16**, 1–46. (doi:10.1016/0040-1951(73)90129-7)

52. Arneodo A, Bacry E, Muzy JF. 1995 The thermodynamics of fractals revisited with wavelets. *Physica A* **213**, 232–275. (doi:10.1016/0378-4371(94)00163-N)
53. Mandelbrot B. 1982 *The fractal geometry of nature*. San Francisco, CA: W.H. Freeman.
54. Carlson CA. 1991 Spatial distribution of ore deposits. *Geology* **19**, 111–114. (doi:10.1130/0091-7613(1991)019<0111:SDOOD>2.3.CO;2)
55. Blenkinsop TG. 1994 The fractal dimension of gold deposits: two examples from the Zimbabwe Archaean craton. In *Fractal and dynamic systems in geosciences* (ed. JH Kruhl), pp. 247–258. Berlin, Germany: Springer.
56. Agterberg FP. 1995 Multifractal modelling of the sizes and grades of giant and supergiant deposits. *Int. Geol. Rev.* **37**, 1–8. (doi:10.1080/00206819509465388)
57. Ford A, Blenkinsop TG. 2009 An expanded de Wijs model for multifractal analysis of mineral production data. *Miner. Deposita* **44**, 233–240. (doi:10.1007/s00126-008-0213-3)
58. Liu H, Wang Q, Li G, Wan L. 2012 Characterization of multi-type mineralizations in the Wandongshan gold poly-metallic deposit, Yunnan (China), by fractal analysis. *J. Geochem. Explor.* **122**, 20–33. (doi:10.1016/j.jexplo.2012.05.009)
59. Sun T, Liu L. 2014 Delineating the complexity of Cu–Mo mineralisation in a porphyry copper intrusion by computational and fractal modelling: a case study of the Chehugou deposit in the Chifeng district, Inner Mongolia, China. *J. Geochem. Explor.* **144**, 128–143. (doi:10.1016/j.jexplo.2014.02.015)
60. Cheng Q. 2008 GIS based fractal and multifractal methods for mineral deposit prediction. In *Nonlinear theory and power-law models for information integration and mineral resources quantitative assessments*. Progress in Geomathematics (eds G Bonham-Carter, Q Cheng), pp. 185–225. Berlin, Germany: Springer.
61. Carranza EJM. 2009 Controls on mineral deposit occurrence inferred from analysis of their spatial pattern and spatial association with geological features. *Ore Geol. Rev.* **35**, 383–400. (doi:10.1016/j.oregeorev.2009.01.001)
62. Wang G, Carranza EJM, Zuo R, Hao Y, Du Y, Pang Z, Sun Y, Qu J. 2012 Mapping of district-scale potential targets using fractal models. *J. Geochem. Explor.* **122**, 34–46. (doi:10.1016/j.jexplo.2012.06.013)
63. Yuan F, Li X, Zhou T, Deng Y, Zhang D, Xu C, Zhang R, Jia C, Jowitt SM. 2015 Multifractal modelling-based mapping and identification of geochemical anomalies associated with Cu and Au mineralization in the NW Junggar area of northern Xinjiang Province, China. *J. Geochem. Explor.* **154**, 252–264. (doi:10.1016/j.jexplo.2014.11.015)
64. Wang Q, Deng J, Liu H, Yang L, Wan L, Zhang R. 2010 Fractal models for ore reserve estimation. *Ore Geol. Rev.* **37**, 2–14. (doi:10.1016/j.oregeorev.2009.11.002)
65. Turcotte DL. 1986 A fractal approach to the relationship between ore grade and tonnage. *Econ. Geol.* **81**, 1528–1532. (doi:10.2113/gsecongeo.81.6.1528)
66. Ord A, Hobbs BE, Lester DR. 2012 The mechanics of hydrothermal systems: I. Ore systems as chemical reactors. *Ore Geol. Rev.* **49**, 1–44. (doi:10.1016/j.oregeorev.2012.08.003)
67. Lester DR, Ord A, Hobbs BE. 2012 The mechanics of hydrothermal systems: II. Fluid mixing and chemical reactions. *Ore Geol. Rev.* **49**, 45–71. (doi:10.1016/j.oregeorev.2012.08.002)
68. Bohr T, Tel T. 1988 The thermodynamics of fractals. In *Directions in chaos* (ed. B-L Hao), pp. 194–237. Singapore: World Scientific.
69. Lynch S. 2007 *Dynamical systems with applications using Mathematica®*. Basel, Switzerland: Birkhauser.
70. Feder J. 1988 *Fractals*. New York, NY: Plenum.
71. Sprott JC. 2003 *Chaos and time series analysis*, 507 pp. Oxford, UK: Oxford University Press.
72. Takens F. 1981 Detecting strange attractors in turbulence. In *Dynamical systems and turbulence*. Lecture Notes in Mathematics, vol. 898 (eds D Rand, L-S Young), pp. 366–381. Berlin, Germany: Springer.
73. Vasconcelos DB, Lopes SR, Viana RL, Kurths J. 2006 Spatial recurrence plots. *Phys. Rev. E* **73**, 056207. (doi:10.1103/PhysRevE.73.056207)
74. Webber Jr CL. 2012 README_2012.PDF (Introduction to Recurrence Quantification Analysis, v 14.1). See <http://homepages.luc.edu/~cwebber>.
75. Kononov E. 2006 VRA Visual Recurrence Analysis. Version 4.9. See <http://web.archive.org/web/20070131023353> and <http://www.myjavaserver.com/~nonlinear/vra/download.html>.

76. Thiele ST, Micklethwaite S, Bourke P, Verrall M, Kovesi P. 2015 Insights into the mechanics of en-echelon sigmoidal vein formation using ultra-high resolution photogrammetry and computed tomography. *J. Struct. Geol.* **77**, 27–44. (doi:10.1016/j.jsg.2015.05.006)
77. Hobbs BE, Archibald NJ, Etheridge MA, Wall VJ. 1984 Tectonic history of the Broken Hill Block, Australia. In *Precambrian tectonics illustrated* (eds A Kroöner, R Greiling), pp. 353–368. Stuttgart, Germany: E. Schweizerbartsche.
78. Stemler T, Judd K. 2009 A guide to using shadowing filters for forecasting and state estimation. *Physica D* **238**, 1260–1273. (doi:10.1016/j.physd.2009.04.008)